Rheology of three-dimensional packings of aggregates: Microstructure and effects of nonconvexity

Emilien Azéma,[1,*] Farhang Radjaï,[1,†] Baptiste Saint-Cyr,[1,2] Jean-Yves Delenne,[3] and Philippe Sornay[2]
[1]*Université Montpellier 2, CNRS, LMGC, Cc 048, Place Eugène Bataillon, F-34095 Montpellier Cedex 05, France*
[2]*CEA, DEN, DEC, SPUA, LCU, F-13108 St. Paul lez Durance, France*
[3]*IATE, UMR 1208 INRA-CIRAD-Montpellier Supagro-UM2, 2 place Pierre Viala, F-34060 Montpellier Cedex 01, France*
(Received 11 February 2013; published 22 May 2013)

We use three-dimensional contact dynamics simulations to analyze the rheological properties of granular materials composed of rigid aggregates. The aggregates are made from four overlapping spheres and described by a nonconvexity parameter depending on the relative positions of the spheres. The macroscopic and microstructural properties of several sheared packings are analyzed as a function of the degree of nonconvexity of the aggregates. We find that the internal angle of friction increases with the nonconvexity. In contrast, the packing fraction first increases to a maximum value but declines as the nonconvexity increases further. At a high level of nonconvexity, the packings are looser but show a higher shear strength. At the microscopic scale, the fabric and force anisotropy, as well as the friction mobilization, are enhanced by multiple contacts between aggregates and interlocking, thus revealings the mechanical and geometrical origins of shear strength.

DOI: 10.1103/PhysRevE.87.052205 PACS number(s): 45.70.−n, 83.80.Fg, 61.43.−j

I. INTRODUCTION

Particle shape is a major parameter for the rheological properties of granular materials such as their shear strength, flowability, and packing structure. However, recent research has mostly focused on the complex rheology and micromechanical properties of granular materials by considering simple shapes such as disks and spherical particles. More realistic materials composed of nonspherical particles now have begun to be investigated in experiments and discrete element numerical simulations [1–14]. This interest is motivated by new challenges in civil engineering and powder technology where most processes need to be optimized or revised following the dramatic degradation of natural resources [5,10,15–19]. Realistic particle shapes also raiseo fundamental issues. In particular, it is essential to understand to what extent our present understanding of the rheology of granular materials based on model packings can be extended to complex granular materials for the understanding of the behavior and primary mechanisms at the natural scale of particles and their interactions.

Most granular materials are found with particles of various degrees of sphericity, elongation, angularity, facetedness, and convexity. A general observation is that angular and elongated particles present a higher shear strength than spherical particles [8,11,19–24]. But only recently was it evidenced by systematic simulations that the shear strength is an increasing linear function of elongation [25,26], whereas it first increases with particle angularity up to a maximum value and then saturates as the particles become more angular [27,28]. In contrast, the packing fraction varies nonmonotonically with elongation as, for example, in packings of ellipsoidal shapes [4,25,29–31]. In all reported cases, the networks resulting from various shapes appear to be complex and hardly amenable to simple statistical modeling.

A systematic study is now possible not only due to the available computer power and memory required for contact detection algorithms between complex shapes [23,32–34], but also because recent investigations have shown that simple parameters can be defined to generate particle shapes with continuously variable shape parameters. Among others, the shape parameter η, describing the degree of distortion from a perfectly circular or spherical shape, was used successfully recently in two dimensions to analyze several packings composed of elongated (rounded-cap rectangles) [25,35], angular (irregular hexahedra) [26], and nonconvex (aggregates of overlapped disks) shapes [36,37]. The shear strength and packing fraction for all these particle shapes are mainly controlled by η so that the effect of the parameters specific to each shape (angularity, nonconvexity, elongation) may be considered to be of second order as compared to η [38].

In this paper, we investigate granular materials composed of nonconvex particles in three dimensions. Nonconvex particles are of special interest because the collective behavior of such particles has only been studied in two dimensions [36,37,39] and also because they give rise to a rich microstructure where a pair of particles can interact at several contact points (multiple contacts), leading to the possibility of interlocking between particles. The nonconvexity may affect the behavior through various mechanisms such as the resulting microstructure (contact network and compactness), hindrance of particle rotations due to interlocking, enhanced mobilization of friction, and multiple contacts between particles with an effect similar to that of face-face contacts between angular particles [22,27,28,40].

We consider rigid aggregates of four overlapping spheres with a fourfold rotational symmetry (see Fig. 1). Their nonconvexity can be tuned by adjusting the overlap, the range of shapes thus varying from a sphere, for a full overlap of the four spheres, to an aggregate of four tangent spheres. We focus on the quasistatic behavior and analyze the underlying microstructure with increasing level of nonconvexity. We also compare our data with two-dimensional results for aggregates of three overlapped disks.

In the following, we first introduce in Sec. II the technical details of the simulations and procedures for sample preparation. In Sec. III we present the evolution of shear stress and

*emilien.azema@univ-montp2.fr
†franck.radjai@univ-montp2.fr

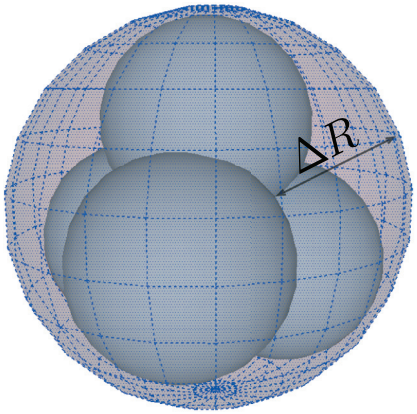

FIG. 1. (Color online) Geometry of a regular aggregate.

packing fraction with shear strain and at an increasing level of nonconvexity. Sections IV and V are devoted to the analysis of contact network topology, force distributions, friction mobilization, and force-contact anisotropy. We conclude with a discussion of the most salient results of this work.

II. MODEL DESCRIPTION

Simulations were carried out by means of the contact dynamics method [41–43]. The contact dynamics method is a discrete element approach for the simulation of nonsmooth granular dynamics with contact laws expressing mutual exclusion and dry friction between particles and an implicit time integration scheme. Hence, this method is numerically unconditionally stable and particularly adapted for the simulation of frictional contacts between particles. It has been extensively employed for the simulation of granular materials in two and three dimensions [5,10,11,22,24,25,27,35,44–51].

The particles are regular aggregates of fourfold rotational symmetry composed of four overlapping spheres of the same radius r as shown in Fig. 1. This shape can be easily characterized by the ratio $\lambda = l/2r$, where l is the distance between the centers of spheres. This parameter varies from 0, corresponding to a sphere, to $\sqrt{3}/2$, corresponding to an aggregate where three coplanar spheres intersect at a single point, so that the radius R of the circumscribing sphere is given by $R = r(1 + \lambda\sqrt{3/2})$.

The aggregates may also be characterized by their nonconvexity, i.e., their degree of distortion η from a perfectly spherical shape, defined as [25,35,38]

$$\eta = \frac{\Delta R}{R}, \tag{1}$$

where $\Delta R = R - R'$, and R' is the radius of the inscribed circle. ΔR can be seen as the concavity of the aggregate. The parameter η has been used to analyze the effect of particle shape on the quasistatic rheological parameters of assemblies of elongated, angular, and nonconvex particles in two dimensions [25,26,35–38] as well as for platy particles in three dimensions [52].

We prepared eight different packings of 12 000 aggregates, with η varying from 0 to 0.7 in steps of 0.1. In order to avoid long-range ordering in the limit of small values of η, we introduce a size polydispersity by taking R in the range $[R_{\min}, R_{\max}]$,

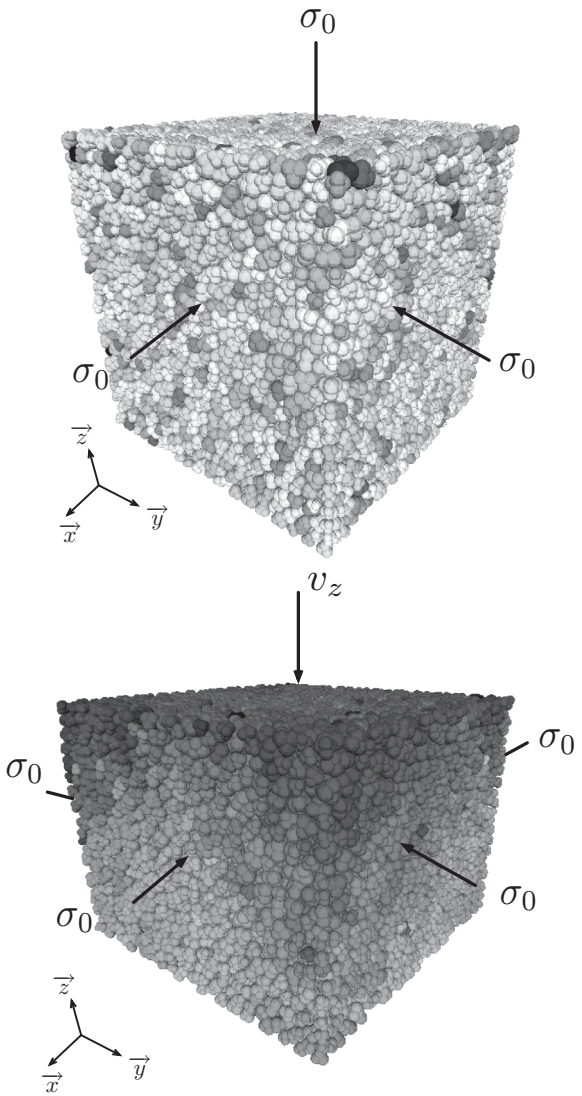

FIG. 2. Boundary conditions for (a) isotropic and (b) triaxial compaction. The gray levels are proportional (a) to particle pressures and (b) to particle velocities at $\varepsilon_q = 0.15$.

with $R_{\max} = 3R_{\min}$, with a uniform distribution of particle volume fractions, which leads to a high packing fraction.

A dense packing composed of spheres is first constructed by means of a layer-by-layer deposition model based on simple geometrical rules [54]. The particles are deposited sequentially on a substrate. For other values of η, the same packing is used, with each sphere serving as the circumscribing sphere of aggregates. The aggregates are inscribed with the given value of η and random orientation in the sphere.

Following this geometrical process, each packing is compacted by isotropic compression inside a box of dimensions $L_0 \times l_0 \times H_0$ in which the left, bottom, and back walls are fixed and the top, right, and front walls are subjected to the same compressive stress σ_0 [see Fig. 2(a)]. The gravity g and the friction coefficient between particles and with the walls are set to 0 during the compression in order to obtain isotropic dense packings.

The isotropic samples are then subjected to vertical compression by downward displacement of the top wall at a

constant velocity v_z for a constant confining stress σ_0 acting on the side walls. This is illustrated in Fig. 2(b) at 15% vertical deplacement of the upper wall. The friction coefficient between particles is set to 0.4 and to 0 with the walls. Since we are interested in quasistatic behavior, the shear rate should be such that the kinetic energy supplied by shearing is negligible compared to the static pressure. This can be formulated in terms of an inertia parameter I defined by [55]

$$I = \dot{\varepsilon}\sqrt{\frac{m}{d\sigma_0}}, \tag{2}$$

where $\dot{\varepsilon} = v_z/z$ and m is the mean particle mass. The rate-independent regime, corresponding to a quasistatic behavior, is characterized by $I < 10^{-3}$, which is the case in our simulations [53].

III. MACROSCOPIC BEHAVIOR

A. Definition of macroscopic parameters

In numerical simulations, the stress tensor can be evaluated from the contact forces and geometrical configuration of the packing. Based on the virtual power formalism, an "internal moment" $\boldsymbol{M}$ can be defined for each particle i [41],

$$M^i_{\alpha\beta} = \sum_{c\in i} f^c_\alpha r^c_\beta, \tag{3}$$

where f^c_α is the α component of the force exerted on particle i at the contact c, r^c_β is the β component of the position vector of the same contact c, and the summation runs over all contact neighbors of particle i (noted briefly as $c \in i$). Then it can be shown that the internal moment of a collection of rigid particles is the sum of the internal moments of individual particles, and the stress tensor $\boldsymbol{\sigma}$ in a given volume V is simply the density of the internal moment [41,48],

$$\boldsymbol{\sigma} = \frac{1}{V}\sum_{i\in V}\boldsymbol{M}^i = \frac{1}{V}\sum_{c\in V} f^c_\alpha \ell^c_\beta, \tag{4}$$

where $\boldsymbol{\ell}^c$ is the branch vector joining the centers of the two touching particles at contact point c. Note that the first summation runs over all particles, whereas the second summation runs over the contacts (each contact appearing once).

Under triaxial conditions with vertical compression, we have $\sigma_1 \geqslant \sigma_2 = \sigma_3$, where the σ_α are the stress principal values. The mean stress p and stress deviator q are defined by

$$p = (\sigma_1 + \sigma_2 + \sigma_3)/3, \tag{5}$$

$$q = (\sigma_1 - \sigma_3)/3. \tag{6}$$

For our system of perfectly rigid particles, the stress state is characterized by the mean stress p and the normalized shear stress q/p.

The cumulative strain components ε_α are defined by

$$\varepsilon_1 = \int_{H_0}^{H}\frac{dH'}{H'} = \ln\left(1+\frac{\Delta H}{H_0}\right), \tag{7}$$

$$\varepsilon_2 = \int_{L_0}^{L}\frac{dL'}{L'} = \ln\left(1+\frac{\Delta L}{L_0}\right), \tag{8}$$

$$\varepsilon_3 = \int_{l_0}^{l}\frac{dl'}{l'} = \ln\left(1+\frac{\Delta l}{l_0}\right), \tag{9}$$

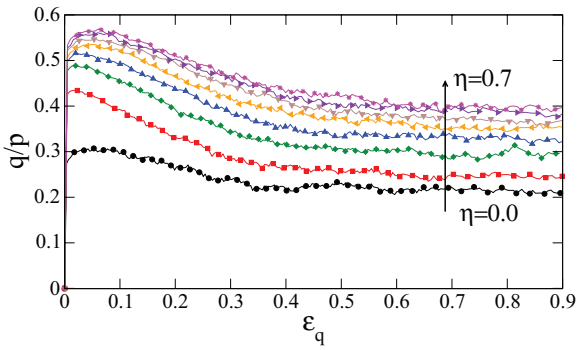

FIG. 3. (Color online) Normalized shear stress q/p as a function of the cumulative shear strain ε_q for all samples with increasing nonconvexity η.

where H_0, l_0, and L_0 are the initial height, width, and length of the simulation box, respectively, and $\Delta H = H_0 - H$, $\Delta l = l_0 - l$, and $\Delta L = L_0 - L$ are the corresponding cumulative displacements. The volumetric strain is given by

$$\varepsilon_p = \varepsilon_1 + \varepsilon_2 + \varepsilon_3 = \int_{V_0}^{V}\frac{dV'}{V'} = \ln\left(1+\frac{\Delta V}{V_0}\right), \tag{10}$$

where V_0 is the initial volume and $\Delta V = V - V_0$ is the total volume change. The cumulative shear strain is defined by

$$\varepsilon_q \equiv \varepsilon_1 - \varepsilon_3. \tag{11}$$

We note that the choice of the deviatoric stress variable q in Eq. (6) with a prefactor of $1/3$ results from the requirement that the total power $\dot{W} = \sigma_1\dot{\varepsilon}_1 + \sigma_2\dot{\varepsilon}_2 + \sigma_3\dot{\varepsilon}_3$ should be expressed as a sum of the products of the volumetric and deviatoric conjugate variables $\dot{W} = p\,\dot{\varepsilon}_p + 2\,q\,\dot{\varepsilon}_q$.

B. Shear strength

Figure 3 displays the normalized shear stress q/p as a function of ε_q for all values of η. Due to the initial isotropic compaction, q/p is nearly 0 in the initial state ($\varepsilon_q = 0$). Then, as we assume that the particles are perfectly rigid and because of the high packing fraction, the shear strength jumps to a peak stress before relaxing to a constant plateau called the "residual" state. We see that the value q/p at the peak and residual states increases with η. The normalized residual stress $(q/p)^*$ is independent of the initial state, and it represents the intrinsic shear strength of the material corresponding to the internal angle of friction φ^* given in three dimensions by

$$\sin\varphi^* = \frac{3(q/p)^*}{2+(q/p)^*}. \tag{12}$$

Figure 4 shows the variation of $(q/p)^*$ and $\sin\varphi^*$ averaged in the residual state as a function of η. The error bars represent the standard deviation computed from the fluctuations around the mean in the residual state in the interval $\varepsilon_q \in [0.5,0.9]$ as shown in Fig. 3. We see that $(q/p)^*$ and $\sin\varphi^*$ increase with η at a decreasing rate. This increase in shear strength reflects the effect of interlocking due to particle nonconvexity as we see in Sec. IV. In a recent work, the quasistatic rheology of granular packings of elongated [25,27], angular [26], and nonconvex particles [36,37] in two dimensions was systematically analyzed by means of the parameter η. A similar

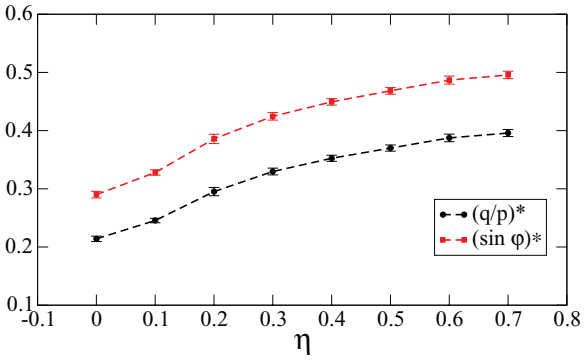

FIG. 4. (Color online) Normalized shear stress $(q/p)^*$ [(black) circles] and friction angle $(\sin\varphi)^*$ [(red) squares] averaged in the residual state as a function of the nonconvexity parameter η.

ascending trend of shear strength with a trend to saturation was found as a function of η, showing that this low-order parameter is a generic shape parameter, underlying, to a large extent, the effect of particle shape.

C. Packing fraction

In Fig. 5, the evolution of packing fraction ρ is shown as a function of ε_q for all values of η. All samples dilate during shear and ρ declines from its value ρ^0 in the initial isotropic state down to a constant value ρ^* in the residual state. The samples dilate almost homogeneously at low shear strains ($\leqslant 0.3$) and thus ρ decreases rapidly. At larger strains, dilation is localized within shear bands appearing throughout the system. Figure 6 shows a gray level map of particle velocities in a portion of packing for $\eta = 0.6$ at $\varepsilon_q = 0.65$, revealing the shear band in the material. As the shear bands develop inside the system, different locations of the sample dilate at different times, and a nearly homogeneous density ρ^* is reached only at $\varepsilon_q = 0.5$. For our rigid particles the residual packing fraction ρ^* is independent of the confining pressure and it should be considered as an intrinsic property of the material, i.e., reflecting basically the particle shape and size distribution as well as the friction coefficient between particles.

Figure 7 displays ρ_0 and ρ^* as a function of η. Remarkably, in both cases, the packing fraction first grows from its value for spheres ($\eta = 0$) towards a maximum at $\eta = 0.3$ and then declines at higher values of η. The peak value of packing

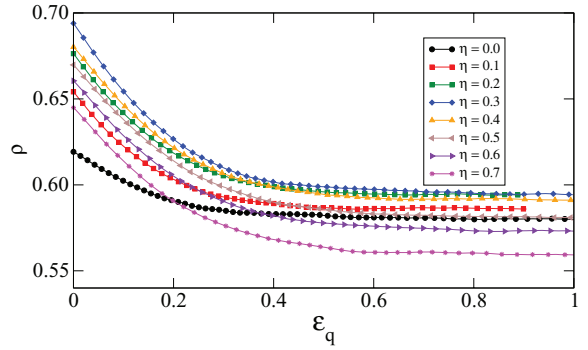

FIG. 5. (Color online) Evolution of the packing fraction ρ with the cumulative shear strain ε_q for different values of η.

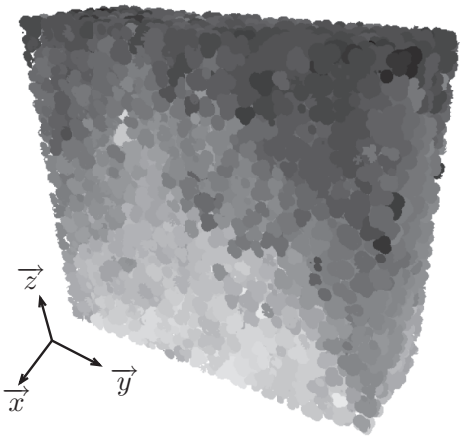

FIG. 6. Gray level map of particle velocities in a portion of the packing at $\varepsilon_q \simeq 0.65$ for $\eta = 0.6$.

fraction ρ_0 in the isotropic state is as high as 0.70. In the residual state, the packing fraction ρ^* takes values as low as 0.55 at $\eta = 0.7$. This nonmonotonic variation of the packing fraction as a function of the nonconvexity shows the complexity of granular textures created by nonspherical particles. On intuitive grounds, it might be expected that with an increase in nonconvexity, the packing fraction would increase as a result of reinforced interlocking between particles. This is clearly not the prevailing mechanism in the range $\eta > 0.3$.

A similar nonmonotonic behavior of the packing fraction was previously observed for granular packings composed of nonconvex particles in two dimensions [36–38], as well as for elongated particles such as ellipses, ellipsoidal particles, spherocylinders, and rounded-cap rectangles [4,25,29–31]. For elongated particles, the falloff in the packing fraction at higher aspect ratios is attributed to the increase in the largest pore volume that cannot be filled by a particle. A similar effect can be advocated for our nonconvex particles, which can form an increasingly tortuous and large pore space as the nonconvexity increases.

IV. GRANULAR TEXTURE

A. Contact and neighbors network topology

In this section, we investigate the general organization (texture) of our packings in terms of particle connectivity.

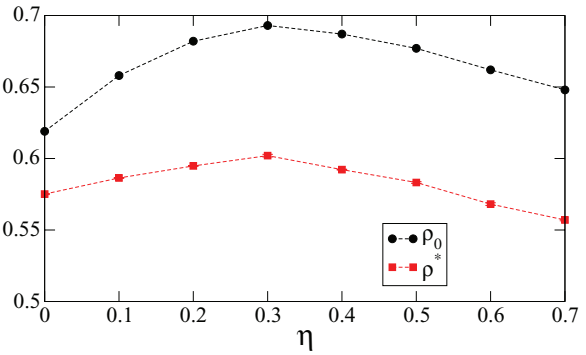

FIG. 7. (Color online) Packing fraction ρ as a function of η both in the initial isotropic state [(black) circles] and in the residual state [(red) squares].

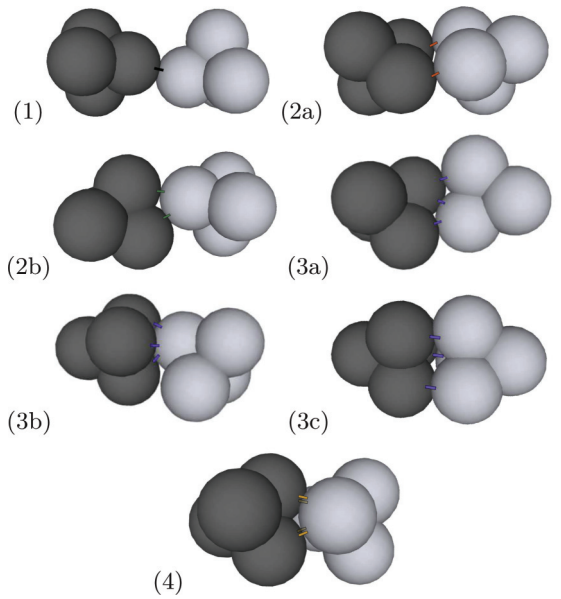

FIG. 8. Contact configurations between two particles: (1) "simple" (s) contacts, (2a) "double-simple" (ds) contacts, (2b) "double" (d) contacts (d), (3a, 3b, 3c) "triple" (t) contacts, and (4) "quadruple" (q) contacts.

The main effect of shape nonconvexity is to allow for multiple contacts between aggregates as shown in Fig. 8. Seven types of contacts can occur between two particles: (i) "simple" (s) contacts; (ii) "double-simple" (ds) contacts, defined as two simple contacts between two pairs of spheres; (iii) "double" (d) contacts, defined as two contacts between one sphere of one aggregate and two spheres belonging on the other aggregate; (iv) "triple" (t) contacts, defined as a combination of simple and double contacts or one sphere of one aggregate and three spheres of another aggregate or three simple contacts; (v) "quadruple" (q) contacts, defined as a combination of two double contacts, and (vi) five or six contacts with a negligible proportion (below 1%) compared to other contact types.

Thus, given multiple contacts between aggregates, we can distinguish between the coordination number Z, the mean number of neighbors per particle (multiple contacts seen as one contact), and the "connectivity" number Z_c, defined as the mean number of contacts per particle. For spherical particles we have $Z = Z_c$. Considering only the contact types s, ds, t, and q and neglecting higher-order contacts, we get

$$\frac{Z_c}{Z} = k_s + 2(k_{ds} + k_d) + 3k_t + 4k_q, \qquad (13)$$

where k_s, k_{ds}, k_d, k_t, and k_q are the proportions of s, ds, d, t, and q contacts, respectively. Figure 9 displays Z and Z_c in the isotropic and residual states as a function of η. The exponents 0 and $*$ refer to the isotropic and residual states, respectively. We see that Z_c^0 jumps from 6 for spheres to $\simeq$12 for $\eta > 0$. This jump is compatible with the isostatic nature of our packings prepared with a zero friction coefficient [56]. Frictionless spheres are characterized by 3 degrees of freedom (df; rotations being immaterial) so that the isostatic condition implies three independent constraints (normal forces), which amounts to a connectivity number of 6. For nonspherical particles, the particle rotations become material and a similar counting

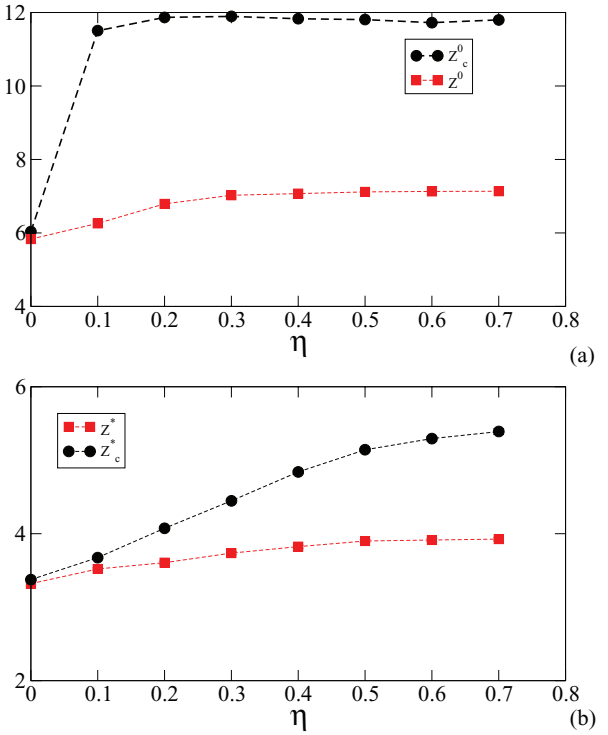

FIG. 9. (Color online) Coordination Z and connectivity Z_c numbers as a function of η in both (a) initial and (b) residual states.

argument leads to a connectivity number of 12. For frictional aggregates, in the residual state, Z_c^* is lower but increases from 3.5 to 5.5 with η. Interestingly, we also see that, in both isostatic and residual states, Z increases much less slowly with η than Z_c. In others words, as in the two-dimensional (2D) case [36,37], the effect of increasing nonconvexity is expressed by an increasing number of multiple contacts with the same average number of neighboring aggregates, and therefore at large values of η the packings are loose but well connected.

To gain further insight into the connectivity of the contact network, we plot in Fig. 10 the proportion of each contact type in the isostatic and residual states as a function of η. We observe that the proportions of different types of connection between aggregates are nearly independent of η in the isostatic state. The simple contacts represent the highest proportion ($\simeq$0.56), whereas ds, t, and q contacts have the lowest proportions ($\leqslant$0.15). The d contacts are represented by an intermediate proportion of nearly 0.3. In the residual state, the proportion of simple contacts declines as η is increased but its value remains above that in the isotropic state, at the expense of the increasing number of other contact types, which are fewer in number.

We also observe a drastic loss of double contacts in the residual state compared to the initial isotropic state for all values of η, whereas the proportions of double-simple and triple contacts are nearly the same and the proportion of quadruple contacts is nearly 0. This can be explained by the fact that the residual state is governed by shear-induced dilation. In this, the particles explore constantly metastable states and thus double and multiple contacts are less involved in the stability of the packing. In contrast, the isostatic state corresponds to the unique minimum of the total potential energy $\sigma_0 V$ of the packing. This state is achieved by the enhanced number of

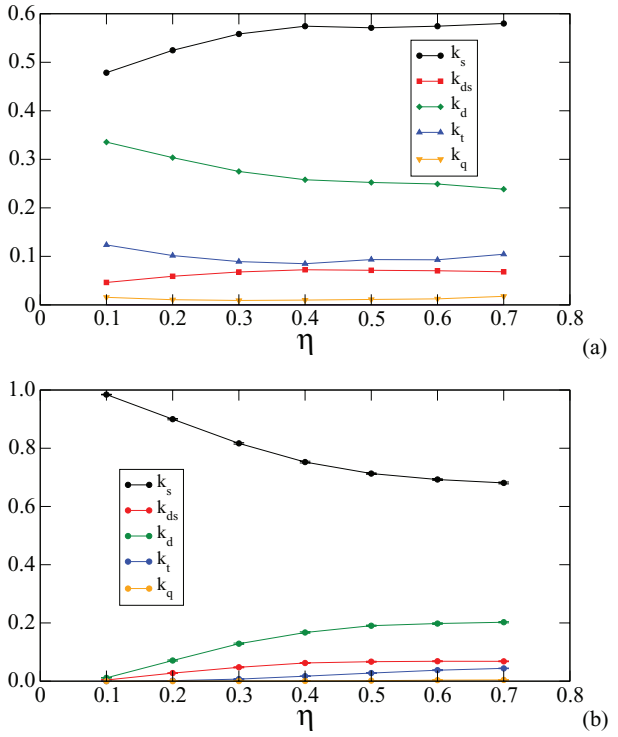

FIG. 10. (Color online) Proportions of simple, double, double-simple, triple, and quadruple contacts as a function of η in the (a) isotropic and (b) residual states.

double and triple contacts, which, by interlocking, contribute to increasing the packing fraction.

The description of the microstructure in terms of the average coordination and connectivity between the aggregates provides a clear picture of the effect of shape nonconvexity. It is also remarkable that the trends observed here by 3D simulations are nearly identical to those observed by Saint-Cyr *et al*. and Szarf *et al*. by means of 2D simulations [36,37]. In the following, we analyze higher order descriptors of the microstructure and their relationship to the macroscopic behavior.

B. Fabric and branch-length anisotropy

A well-known feature of dry granular materials is that the shear strength is related to the buildup of an anisotropic structure during shear due to (i) friction between the particles and (ii) as a result of steric effects depending on particle shape [57]. A common approach used by various authors is to consider the probability distribution $P(\boldsymbol{n})$, where $\boldsymbol{n}$ is the unit vector of contact normals in the *contact frame* $(\boldsymbol{n},\boldsymbol{t})$, with $\boldsymbol{t}$ an orthonormal unit vector oriented along the tangential force as illustrated in Fig. 11(a). In three dimensions, let $\Omega = (\theta,\phi)$ be the angles that define the orientation of $\boldsymbol{n}$, where θ is the radial angle and ϕ the azimutal angle as defined in Fig. 11(c). From numerical data we can then evaluate the probability density functions $P_\Omega(\Omega)$ of contacts pointing along a direction Ω.

We have seen previously that, due to multiple contacts between nonconvex particles, the contact network is different from the network of neighboring particles. Thus, in addition to the distribution $P(\boldsymbol{n})$ of contact normals $\boldsymbol{n}$, we define the probability distribution $P(\boldsymbol{n}')$ for the neighbor network, where

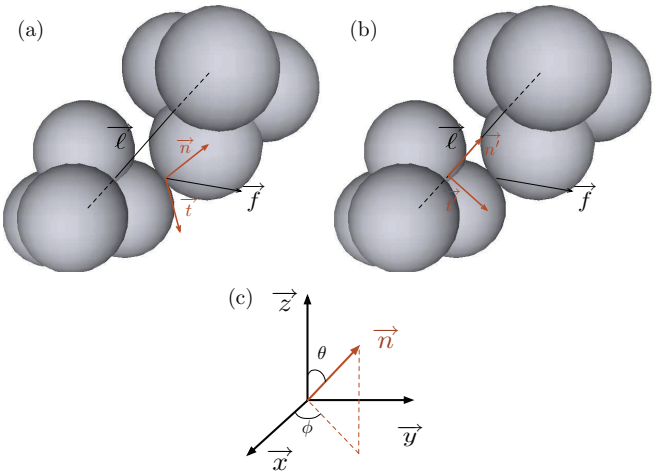

FIG. 11. (Color online) (a) Contact frame $(\boldsymbol{n},\boldsymbol{t})$; (b) intercenter frame $(\boldsymbol{n}',\boldsymbol{t}')$; (c) azimutal angle Φ and radial angle Θ.

$\boldsymbol{n}'$ is the unit *branch vector* joining the centers of two touching aggregates and pointing in a direction $\Omega' = (\theta',\phi')$. We also associate a local frame $(\boldsymbol{n}',\boldsymbol{t}')$, with $\boldsymbol{t}'$ an orthonormal unit vector [see Fig. 11(b)]. Under the axisymmetric conditions of our simulations, P_Ω and $P_{\Omega'}$ are independent of the azimuthal angles ϕ and ϕ' so that we may consider in the following only the probability densities P_θ and $P_{\theta'}$ of the radial angles θ and θ'.

The inset in Fig. 12 displays a polar representation of the above functions in the θ plane in the critical state for $\eta = 0.4$. We observe an anisotropic behavior in all cases. The peak value occurs along the compressive axis ($\theta_c = \theta_c' = \pi/2$) and coincides with the principal stress direction $\theta_\sigma = \pi/2$. The peak is less marked for $P_{\theta'}$ than for P_θ. The simple shapes of the above functions suggest that the harmonic approximation based on spherical harmonics at leading terms captures the anisotropies of both neighbor and contact networks. There are nine second-order basis functions $Y_m^l(\Theta,\Phi)$ [11,28], where (Θ,Φ) stands either for (θ,ϕ) or for (θ',ϕ'),

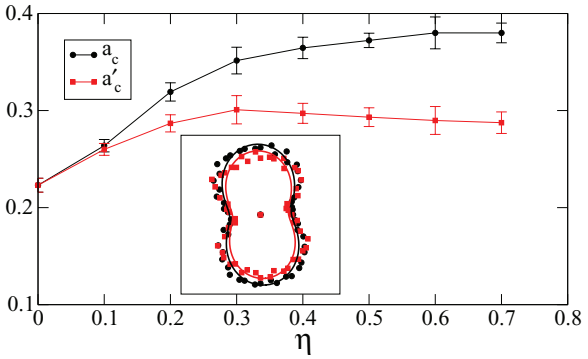

FIG. 12. (Color online) Contact anisotropy a_c [(black) circles] and branch vector anisotropy a_c' [(red) squares] as a function of the shape parameter η averaged in the residual state. Error bars represent the standard deviation in the residual state. Inset: Angular probability densities $P_\theta(\theta)$ [(black) circles] and $P_{\theta'}(\theta')$ [(red) squares] for $\eta = 0.4$ calculated from the simulations (data points) together with the harmonic approximation (lines).

depending on the local frame used, but only the functions compatible with the symmetries of the problem (i.e., independent with respect to Φ and π-periodic with Θ) are admissible. The only admissible functions are therefore $Y_0^0 = 1$ and $Y_2^0 = 3\cos^2\Theta - 1$. Hence, within a harmonic model of fabric, we have

$$P_\Theta(\Theta) = \frac{1}{4\pi}\{1 + \bar{a}_c[3\cos^2(\Theta - \Theta_c) - 1]\}, \quad (14)$$

where $(\bar{a}_c,\Theta_c) = (a_c,\theta_c)$ are the contact anisotropy and the privileged contact direction of the contact network and $(\bar{a}_c,\Theta_c) = (a_c',\theta_c')$ are the branch anisotropy and the privileged branch direction of the neighbor network. In practice, the values of $\bar{a}_c$ can be calculated from generalized fabric tensors as described in Ref. [28].

Figure 12 shows the variation of a_c and a_c' averaged in the residual state as a function of η. We see that both anisotropies increase with η from 0.2 to a nearly constant value of 0.3 and 0.36, respectively, beyond $\eta > 0.4$. We also have $a_c' < a_c$. The saturation of a_c' in the residual state is compatible with the saturation of Z, which represents the coordination number of the network of neighbors, as shown in Fig. 9. On the other hand, a_c slightly increases as Z_c with η due to enhanced interlocking and gain of contacts with the same neighboring aggregates (since Z is nearly independent of η in the range $\eta > 0.4$). Hence, the effect of the nonconvexity of the aggregates on the texture manifests itself in increased coordination, connectivity, and contact anistropy in the range $\eta \leqslant 0.4$ and in enhanced connectivity and anisotropy due to interlocking.

This increase in interlocking can also be observed for the projections $\ell_n\boldsymbol{n}$ and $\ell_t\boldsymbol{t}$ of the branch vector $\ell_{n'}\boldsymbol{n'}$ along the normal and tangential forces, respectively. In close correlation with contact and branch anisotropies, we can define the average angular dependance of this quantity. We consider the joint probability density $P(\ell_n,\boldsymbol{n})$, $P(\ell_t,\boldsymbol{t})$, and $P(\ell_{n'},\boldsymbol{n'})$ of the normal, tangential, and radial branch lengths. We have the three expressions

$$\langle\ell_n\rangle(\Omega)P_\Omega(\Omega) = \int_0^\infty \ell_n P(\ell_n,\boldsymbol{n})d\ell_n, \quad (15)$$

$$\langle\ell_t\rangle(\Omega)P_\Omega(\Omega) = \int_0^\infty \ell_t P(\ell_t,\boldsymbol{t})d\ell_t, \quad (16)$$

$$\langle\ell_{n'}\rangle(\Omega')P_{\Omega'}(\Omega') = \int_0^\infty \ell_{n'} P(\ell_{n'},\boldsymbol{n'})d\ell_{n'}, \quad (17)$$

where $\langle\ell_n\rangle(\Omega)$, $\langle\ell_t\rangle(\Omega)$, and $\langle\ell_{n'}\rangle(\Omega')$ are the average normal, tangential, and radial lengths along the directions Ω and Ω', respectively [28] The mean normal, tangential, and radial lengths are simply given by

$$\langle\ell_n\rangle = \frac{1}{4\pi}\int_{\mathcal{S}}\langle\ell_n\rangle(\Omega)P_\Omega(\Omega)d\Omega, \quad (18)$$

$$\langle\ell_t\rangle = \frac{1}{4\pi}\int_{\mathcal{S}}\langle\ell_t\rangle(\Omega)P_\Omega(\Omega)d\Omega, \quad (19)$$

$$\langle\ell_{n'}\rangle = \frac{1}{4\pi}\int_{\mathcal{S}}\langle\ell_{n'}\rangle(\Omega')P_{\Omega'}(\Omega')d\Omega', \quad (20)$$

where $\mathcal{S}$ is the integration domain $[0,\pi]\times[0,2\pi]$. $\langle\ell_n\rangle$ and $\langle\ell_{n'}\rangle$ are always positive by construction. In contrast, ℓ_t can be negative and we get $\langle\ell_t\rangle \sim 0$ in all our simulations. This condition implies that the functions $\langle\ell_t\rangle(\Omega)$ and $P_\Omega(\Omega)$ are orthonormal. Moreover, under the axisymmetric conditions of our simulations, these functions are independent of the azimuthal angles ϕ and ϕ'. These functions can then be expanded at first order over a spherical harmonic basis as follows:

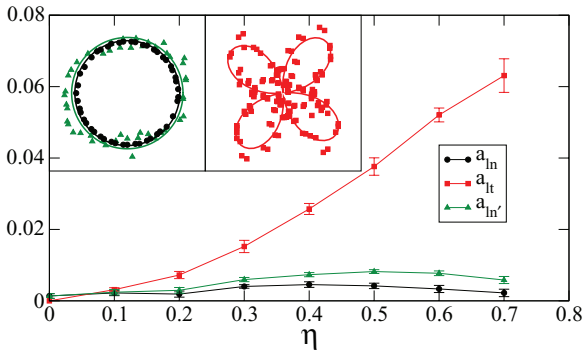

FIG. 13. (Color online) Normal and tangential branch length anisotropies a_{ln} (circles) and a_{lt} (squares) and branch-length anisotropy $a_{ln'}$ (triangles) as a function of the shape parameter η in the residual state. Error bars represent the standard deviation in the residual state. Inset: Angular average functions $\langle\ell_{ln}\rangle(\theta)$ [(black) circles], $\langle\ell_{lt}\rangle(\theta)$ [(red) squares], and $\langle\ell_{ln'}\rangle(\theta)$ [(green) triangles] for $\eta = 0.4$, calculated from the simulation data (points) and approximated by harmonic fits (lines).

$$\langle\ell_{\bar{n}}\rangle(\Theta) = \langle\ell_{\bar{n}}\rangle\{1 + a_{l\bar{n}}[3\cos^2(\Theta - \Theta_{l\bar{n}}) - 1]\}, \quad (21)$$

$$\langle\ell_t\rangle(\theta) = \langle\ell_n\rangle a_{lt}\sin 2(\theta - \theta_{lt}), \quad (22)$$

where $(\ell_{\bar{n}},a_{l\bar{n}},\Theta_{l\bar{n}}) = (\ell_n,a_{ln},\theta_{ln})$ are the normal branch-length anisotropy and privileged orientation of $\langle\ell_n\rangle(\theta)$ in the frame $(\boldsymbol{n},\boldsymbol{t})$, $(\ell_{\bar{n}},a_{l\bar{n}},\Theta_{l\bar{n}}) = (\ell_{n'},a_{ln'},\theta_{ln'})$ are the radial branch-length anisotropy and privileged orientation of $\langle\ell_{n'}\rangle(\theta')$ in $(\boldsymbol{n'},\boldsymbol{t'})$, and (a_{lt},θ_{lt}) are the tangential branch-length anisotropy and the privileged orientation of $\langle\ell_t\rangle(\theta)$ in $(\boldsymbol{n},\boldsymbol{t})$, respectively.

The inset in Fig. 13 shows the polar diagrams of the simulation data for $\langle\ell_n\rangle(\theta)$, $\langle\ell_t\rangle(\theta)$, and $\langle\ell_{n'}\rangle(\theta')$ at $\eta = 0.4$, together with the harmonic approximations in the residual state. We see that the distributions of normal and radial branch length are nearly isotropic, whereas the distribution of tangential branch-length components has two modes along the directions $\theta_t \pm \pi/4$. The variation of normal, tangential, and radial length anisotropies is plotted in Fig. 13 as a function of η. We see that $a_{ln} \sim a_{ln'} \sim 0$. This is due to the absence of shape eccentricity of the particles [25,27,28,35,58,59] and also because of the low span in the particle size distribution [46]. This shows that, even if the particles and contacts are nonuniformly distributed around each particle, the mean distance between particles remains nearly constant. In contrast, we see that a_{lt} increases with η from 0 to 0.06. These values are weak but their global increase is directly related to the increase in interlocking. In fact, the tangential projection of the branch vector ℓ_t on the contact plane between two aggregates increases with interlocking. This leads to the increase in the ratio ℓ_t/ℓ_n for the interlocked aggregates and thus the average value $\langle\ell_t\rangle/\langle\ell_n\rangle$ at $\theta = \theta_{lt} + \pi/4$, which is equal to a_{lt} according to Eq. (22).

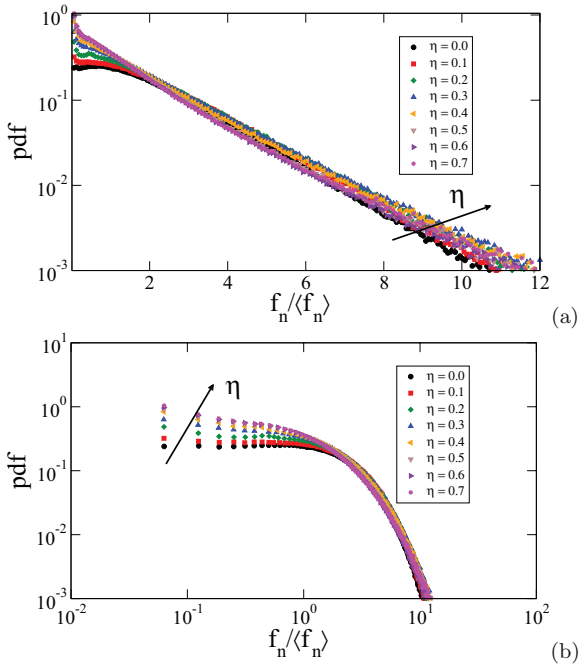

FIG. 14. (Color online) Probability density functions of normal forces on (a) log-linear and (b) log-log scales.

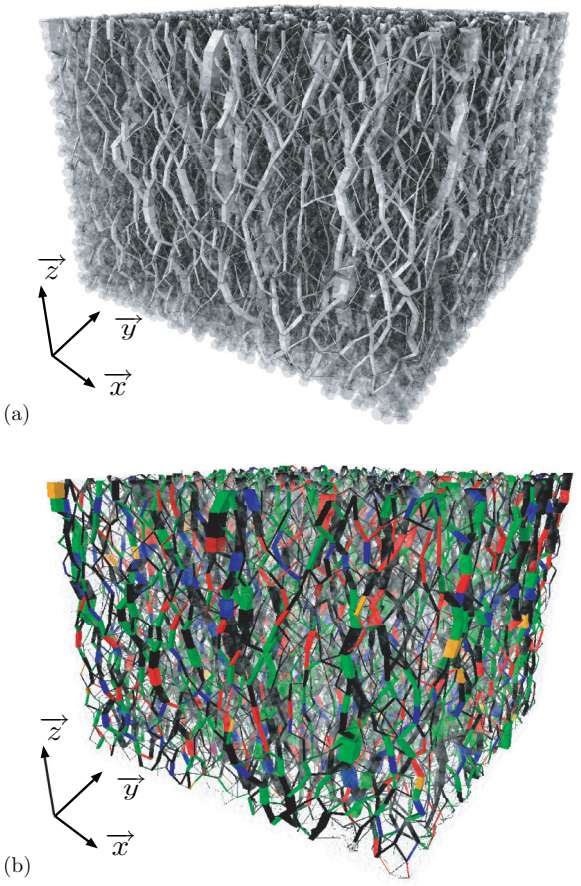

FIG. 15. (Color online) Snapshot of radial forces for $\eta = 0.6$. (a) Line thickness is proportional to the radial force. (b) Forces are plotted in different colors, depending on the contact type: s contacts, black; d contacts, red; ds contacts, green; t contacts, purple; and q contacts, yellow.

V. FORCE TRANSMISSION

A. Force distribution

We consider in this section the distribution of contact forces, which reflects the inhomogeneity of the contact network [47,60–62]. The normal-force probability density functions averaged in the residual state are shown in Fig. 14 on a log-linear [Fig. 14(a)] and log-log [Fig. 14(b)] scale for all values of η. The distribution becomes increasingly broader as the nonconvexity increases but the relative changes are surprisingly small. Indeed, the maximum force varies from $10\times$ the mean force for spheres to $12\times$ the mean force for $\eta = 0.7$. We also observe an increasing number of contacts carrying weak forces (below the mean) as η increases. This rather small change in the distributions with η may be attributed to the fact that the contacts are always between the spheres belonging to the aggregates, and from this viewpoint the distribution of forces is not very different from that for a packing of spheres.

Another way to highlight the role of multiple contacts in force transmission is to consider the reaction forces between aggregates. The reaction force $\boldsymbol{F}$ between two aggregates is the result of point forces acting at their contacts, and it can be projected onto the intercenter frame. In this way, the contact-force network can be replaced by the simplest *neighbor-force* network carrying the radial forces $f_{n'} = \boldsymbol{F}\boldsymbol{n}'$. Figure 15(a) shows the neighbor-force network in the residual state for $\eta = 0.6$. The "force forest" shown in this figure represents the force chains along the branch vectors. Figure 15(b) shows the same snapshot with the radial forces colored according to contact type. It seems that stronger force chains are composed essentially of double and double-simple contacts and occasionally mediated by simple, triple, and quadruple contacts.

The radial-force probability density functions averaged in the residual state are shown in Fig. 16 on log-linear [Fig. 16(a)] and log-log [Fig. 16(b)] scales for all values of η. The distribution becomes broader than contact-force distributions as the nonconvexity is increased. We observe an increasing number of both weak forces and stronger forces. This means that the packings of more nonconvex aggregates, though more closely connected, are more inhomogeneous in terms of radial forces.

The anisotropic structures shown in Fig. 15 can be characterized more generally through the angular dependence of the average normal and radial forces via the same methodology as given in Sec. IV for branch-length orientations. Considering the joint probability densities $P(f_n,\boldsymbol{n})$ and $P(f_{n'},\boldsymbol{n}')$ of the normal and radial forces, we have

$$\langle f_{\bar{n}} \rangle(\bar{\Omega}) P_{\bar{\Omega}}(\bar{\Omega}) = \int_0^\infty f_{\bar{n}} P(f_{\bar{n}},\bar{\Omega}) df_{\bar{n}}, \tag{23}$$

where $(\bar{n},\Theta)$ stands alternatively for (n,θ) in the contact frame or for (n',θ') in the branch frame. $\langle f_n \rangle(\Omega)$ and $\langle f_{n'} \rangle(\Omega')$ are the average normal and radial forces along the directions θ and θ', respectively. The average normal/radial force is given by

$$\langle f_{\bar{n}} \rangle = \frac{1}{4\pi} \int_{\mathcal{S}} \langle f_{\bar{n}} \rangle(\bar{\Omega}) P_{\bar{\Omega}}(\bar{\Omega}) d\bar{\Omega}. \tag{24}$$

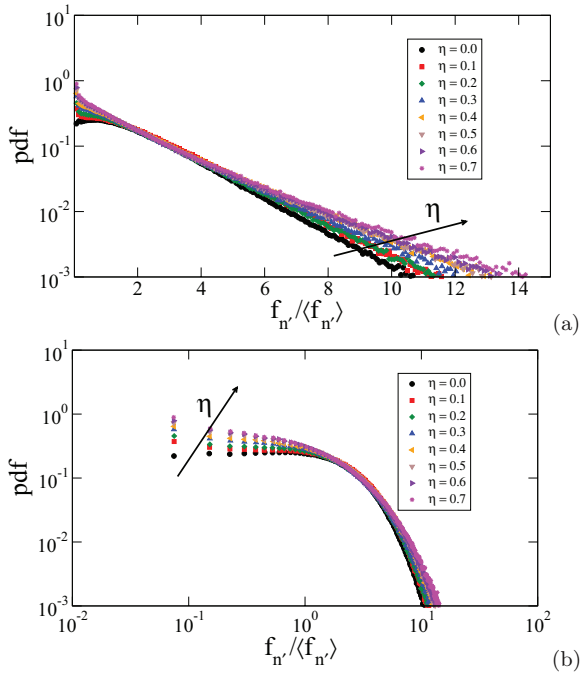

FIG. 16. (Color online) Probability density functions of radial forces on (a) log-linear and (b) log-log scales.

Under the axisymmetric conditions of our simulations, the above probability density functions are independent of the azimuthal angle ϕ and can be expanded on a spherical harmonics basis as

$$\langle f_{\bar{n}}\rangle(\Theta) = \langle f_{\bar{n}}\rangle\{1 + a_{f\bar{n}}[3\cos^2(\Theta - \Theta_{\bar{n}}) - 1]\}, \qquad (25)$$

where $(f_{\bar{n}}, a_{\bar{n}}, \Theta_{\bar{n}}) = (f_n, a_{fn}, \theta_n)$ are the normal-force anisotropy and privileged orientation of $\langle f_n\rangle(\theta)$ in $(\boldsymbol{n},\boldsymbol{t})$, and $(f_{\bar{n}}, a_{\bar{n}}, \Theta_{\bar{n}}) = (f_{n'}, a_{fn'}, \theta_{n'})$ are the radial-force anisotropy and privileged orientation of $\langle f_{n'}\rangle(\theta')$ in $(\boldsymbol{n'},\boldsymbol{t'})$. This form is well fit to the data as shown in the inset in Fig. 17 in the residual state for $\eta = 0.4$. We also see that both θ_n and $\theta_{n'}$ coincide with the principal stress direction $\theta_\sigma = \pi/2$.

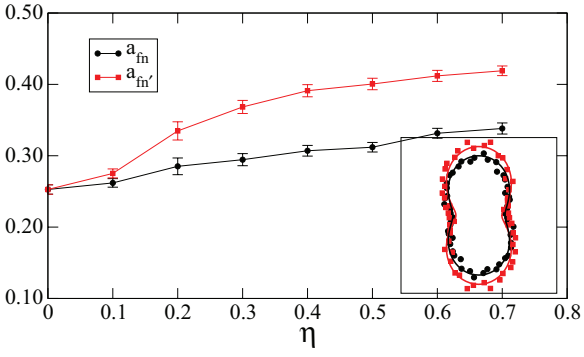

FIG. 17. (Color online) Normal and radial force anisotropies a_{fn} [(black) circles] and $a_{fn'}$ [(red) squares] as a function of η in the residual state. Error bars represent the standard deviation in the residual state. Inset: Angular average functions $\langle f_n\rangle(\theta)$ [(black) circles] and $\langle f_{n'}\rangle(\theta)$ [(red) squares] for $\eta = 0.4$ calculated from the simulation data (points) together with the harmonic approximation (lines). Error bars represent the standard deviation in the residual state.

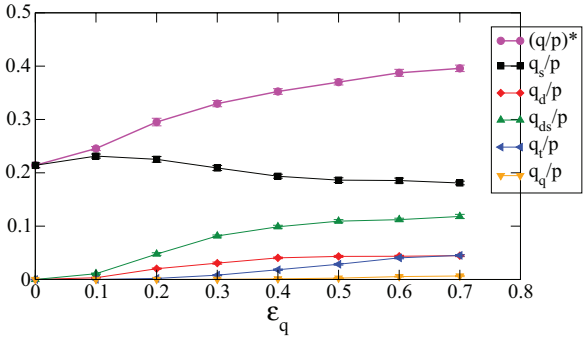

FIG. 18. (Color online) Normalized shear stress supported by s, ds, t, and q contacts as a function of η.

The residual-state values of a_{fn} and $a_{fn'}$ are displayed together in Fig. 17 as a function of η. We see that $a_{fn'} > a_{fn}$ and that both anisotropies increase with η from 0.2 to 0.33 for a_{fn} and to 0.43 for $a_{fn'}$. The large variation of $a_{fn'}$ with η is consistent with the fact that the probability density function of radial forces is increasingly broader with η. Moreover, the increase in a_{fn} and $a_{fn'}$ in connection to the saturation of a_c and a_c' (see Sec. IV), implies that stronger force chains are transmitted through the principal stress direction, while on average the mean orientation of contacts remains unchanged at larger η. This can be attributed to the increase in the proportion of multiple contacts between particles. Indeed, by restricting the summation in Eq. (4) to each contact type, one may partition the stress tensor as a sum of partial stress tensors,

$$\boldsymbol{\sigma} = \boldsymbol{\sigma}_s + \boldsymbol{\sigma}_{ds} + \boldsymbol{\sigma}_d + \boldsymbol{\sigma}_t + \boldsymbol{\sigma}_q, \qquad (26)$$

where $\boldsymbol{\sigma}_s$, $\boldsymbol{\sigma}_{ds}$, $\boldsymbol{\sigma}_d$, $\boldsymbol{\sigma}_t$, and $\boldsymbol{\sigma}_q$ represent the stresses carried by different contact types. The corresponding stress deviators q_s, q_{ds}, q_d, q_t, and q_q averaged in the residual state and normalized by the mean stress p are shown in Fig. 18 as a function of η. It is remarkable that the shear stress q_s/p supported by simple contacts remains nearly independent of η and equal to ∼0.2, whereas the proportion of simple contacts decreases drastically with η, from 1 to 0.65, as shown in Sec. IV. Hence, the increase in shear strength with η is mainly due to the increase in q_d/p and, to a lesser extent, to the other contacts. In this way, the growth of the number of interlocked contacts is clearly at the origin of the enhanced shear strength of the packings as η increases.

B. Friction mobilization

The mobilization of friction forces is a basic parameter in granular materials. A simple way to quantify the friction mobilization in granular materials is to consider the proportion S of sliding contacts, i.e., the contacts where the friction force f_t equals μf_n in absolute value in steady shearing. Figure 19 displays S in the residual state as a function of η. We see that S increases from 0.23 for spheres to 0.7 for $\eta = 0.7$. Another key fact is that the sliding contacts are unevenly distributed among simple, double-simple, double, triple, and quadruple contacts, as shown in Fig. 20. Only a weak number of double-simple, triple, and quadruple contacts are sliding, whereas the proportion of sliding double contacts increases with η at the expense of simple contacts.

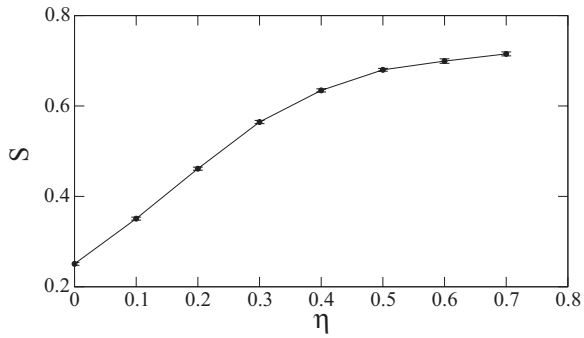

FIG. 19. Proportion of sliding contacts as a function of η in the residual state. Error bars show the standard deviation in the residual state.

A somewhat more elegant way of describing friction mobilization is to consider the proportion of contacts in correlation with the friction force. We consider the probability density of the tangential and orthoradial forces $f_t\boldsymbol{t} = f_n\boldsymbol{n}' - \boldsymbol{f}$ and $f_{t'}\boldsymbol{t}' = f_{n'}\boldsymbol{n}' - \boldsymbol{f}$, respectively, which derive from the joint probability densities $P(f_t,\boldsymbol{t})$ and $P(f_{t'},\boldsymbol{t}')$, of the tangential f_t and orthoradial $f_{t'}$ forces along the directions $\boldsymbol{t}$ and $\boldsymbol{t}'$, respectively. Thus, as for normal and radial forces, we have

$$\langle f_{\bar{t}}\rangle(\bar{\Omega})P_{\bar{\Omega}}(\bar{\Omega}) = \int_0^\infty f_{\bar{t}}P(f_{\bar{t}},\bar{\Omega})df_{\bar{\Omega}}, \tag{27}$$

where $(\bar{t},\Theta)$ stands alternatively for (t,θ) in the contact frame or for (t',θ') in the branch frame. $\langle f_t\rangle(\Omega)$ and $\langle f_{t'}\rangle(\Omega')$ are the average tangential and orthoradial force along the directions θ and θ', respectively. The average tangential/orthoradial radial force is given by

$$\langle f_{\bar{t}}\rangle = \frac{1}{4\pi}\int_{\mathcal{S}}\langle f_{\bar{t}}\rangle(\bar{\Omega})P_{\bar{\Omega}}(\bar{\Omega})d\bar{\Omega}. \tag{28}$$

Noting now that, in quasistatic deformation the force accelerations are negligible so that the forces and force moments acting on the aggregate a are balanced, we have

$$\sum_{c\in a}\boldsymbol{f}^c = 0, \tag{29}$$

$$\sum_{c\in a}\left\{r_n^c f_t^c + r_t^c f_n^c\right\} = 0, \tag{30}$$

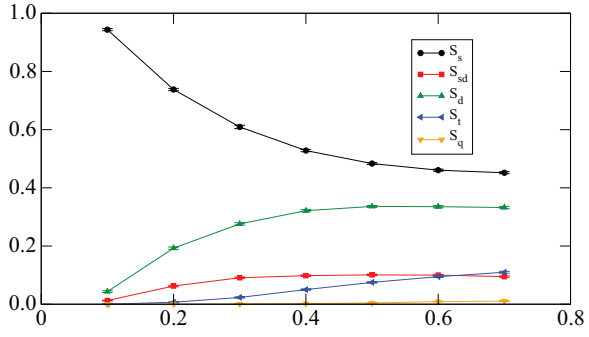

FIG. 20. (Color online) Proportion of sliding contacts as a function of η in the residual state for different contact types. Error bars show the standard deviation in the residual state.

where $r_n^c = \boldsymbol{r}^c\cdot\boldsymbol{n}$ and $r_t^c = \boldsymbol{r}^c\cdot\boldsymbol{t}$, where $\boldsymbol{r}^c$ is the *contact vector* joining the center of inertia of the aggregate a to the contact c. Taking the average of Eq. (30) over all aggregates a, and assuming that ℓ_n, f_t, and ℓ_t, f_n are statistically independent, we get $\langle\ell_n\rangle\langle f_t\rangle = \langle\ell_t\rangle\langle f_n\rangle$. As mentioned in Sec. IV, $\langle\ell_t\rangle = 0$, thus as $\langle\ell_n\rangle > 0$, the average tangential force in the packing vanishes. Similarly, considering the contacts projected onto the branch frame $(\boldsymbol{n}'^c,\boldsymbol{t}'^c)$, we have $\langle f_{t'}\rangle = 0$.

Since the average tangential and orthoradial forces vanish, $\langle f_{\bar{t}}\rangle(\bar{\Omega})$ and $P_{\bar{\Omega}}(\bar{\Omega})$ are orthonormal. Given that under the axisymmetric conditions of our simulations these probability density functions are independent of the azimuthal angle ϕ, these functions can thus be expanded over a spherical harmonics basis as

$$\langle f_t\rangle(\theta) = \langle f_n\rangle a_{ft}\sin 2(\theta-\theta_t), \tag{31}$$

$$\langle f_{t'}\rangle(\theta') = \langle f_{n'}\rangle a_{ft'}\sin 2(\theta-\theta_{t'}), \tag{32}$$

where (a_{ft},θ_t) are the tangential anisotropy and privileged orientation of $\langle f_t\rangle(\theta)$ in the frame $(\boldsymbol{n},\boldsymbol{t})$, and $(a_{ft'},\theta_{t'})$ are the orthoradial anisotropy and privileged orientation of $\langle f_{t'}\rangle(\theta')$ in the frame $(\boldsymbol{n}',\boldsymbol{t}')$.

The inset in Fig. 22 shows polar diagrams of the simulation data for $\langle f_t\rangle(\theta)$ and $\langle f_{t'}\rangle(\theta')$ together with plots of function (31) in the residual state for $\eta = 0.4$. We see that the function fits the data excellently. We also see that $\theta_t = \theta_{t'} = \pi/2$ coincides with the principal stress direction. We thus define a friction mobilization function [28,35],

$$\bar{M}_{\text{fric}}(\Theta) = \frac{\langle f_{\bar{t}}\rangle(\Theta)}{\bar{\mu}\langle f_{\bar{n}}\rangle} = \frac{a_{f\bar{t}}}{\bar{\mu}}\sin 2(\Theta-\Theta_{\bar{t}}), \tag{33}$$

where $\bar{\mu} = \mu$ and $(a_{f\bar{t}},\Theta_{\bar{t}}) = (a_t,\theta)$ in the local contact frame and $\bar{\mu} = \langle(f_{n'}/f_n)\sqrt{(1+\mu^2)-(f_n/f_{n'})^2}\rangle$ and $(a_{f\bar{t}},\Theta_{\bar{t}}) = (a_{t'},\theta')$ in the local neighbor frame. This function has two modes along the directions $\Theta_t \pm \pi/4$ and the ratio $a_{f\bar{t}}/\bar{\mu}$ is simply their amplitude. Hence, integrating Eq. (33) in the range of $[0,\pi]$ we can define an "index" $\bar{I}_{\text{fric}}$ for friction mobilization by

$$\bar{I}_{\text{fric}} = \frac{5}{2\bar{\mu}}a_{f\bar{t}}. \tag{34}$$

The friction mobilization increases from 0 in the isotropic state with shear strain and its value in the residual state depends on the nature of the material. Figure 22 shows a_{ft} and $a_{ft'}$ averaged in the residual state as a function of η. We see that a_{ft} and $a_{ft'}$ increase both from 0.05 to 0.1 and 0.3, respectively, at larger η, in close correlation with the variation of S, indicating that stronger tangential and radial forces are mobilized at larger η. This is what we observe also by visual inspection of Fig. 21, where two maps of radial mobilized friction forces are shown for $\eta = 0.1$ and $\eta = 0.6$ in the residual state.

The force and fabric anisotropies are very interesting descriptors of granular microstructure and force transmission properties, because they underlie the different microscopic origins of shear strength. Indeed, it can be shown that the general expression of the stress tensor [Eq. (4)], together with the spherical harmonics approximation of the texture by Eqs. (14) and (22) and the force network by Eqs. (25) and (31), leads to the following simple expression in both contact-network and neighbor-network

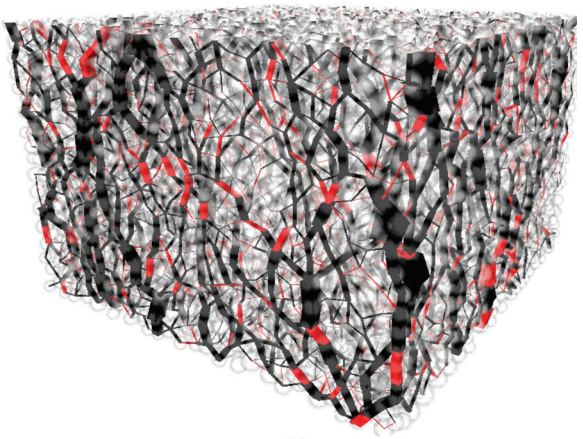

(a)

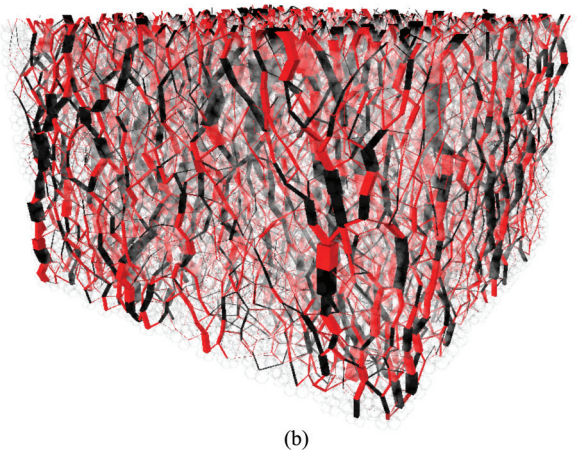

(b)

FIG. 21. (Color online) Map of mobilized forces (in red) for (a) $\eta = 0.1$ and (b) $\eta = 0.7$. The line thickness is proportional to the radial force.

frames [11,25,28,59]:

$$\frac{q}{p} \simeq \frac{2}{5}(a_c + a_{ln} + a_{lt} + a_{fn} + a_{ft}), \tag{35a}$$

$$\frac{q}{p} \simeq \frac{2}{5}(a'_c + a_{ln'} + a_{fn'} + a_{ft'}). \tag{35b}$$

These expressions are based on the following assumptions, which are satisfied with a good approximation in the residual state: (i) The contact forces and branch-vector lengths are weakly correlated; (ii) the reference directions coincide with the major principal stress direction, i.e., $\Theta_c = \Theta_{l\bar{n}} = \theta_{lt} = \Theta_{f\bar{n}} = \Theta_{f\bar{t}} = \theta_\sigma$; and (iii) the cross products among all anisotropies are negligible. Equation (35) is based on general considerations and the values of shear strength given by this equation from the anisotropies are expected to predict correctly the measured shear strength of a packing of nonconvex aggregates too. Note, however, that the second expression given by Eq. (35) is simpler than the first expression (four anisotropy parameters instead of five anisotropy parameters).

Figure 23 shows the normalized shear strength q/p in the residual state together with the two approximations given by Eq. (35). We see that the fit by Eq. (35b) is excellent for all values of η, whereas Eq. (35a) underestimates the shear strength as particle shapes deviate more strongly from the circular shape.

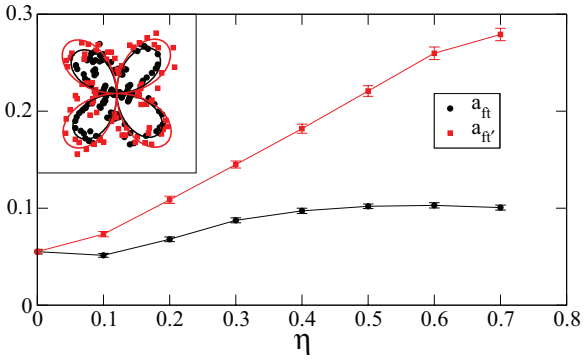

FIG. 22. (Color online) Tangential and orthoradial force anisotropies a_t [(black) circles] and $a_{ft'}$ [(red) squares] as a function of η in the residual state. Error bars represent the standard deviation in the residual state. Inset: Angular average functions $\langle f_t \rangle(\theta)$ [(black) circles] and $\langle f_{t'} \rangle(\theta)$ [(red) squares] for $\eta = 0.4$ calculated from the simulation data (points) together with the harmonic approximation (lines). Error bars represent the standard deviation in the residual state.

A similar result was reported in three dimensions by Ouadfel *et al.* [59] with ellipsoidal particles and by Azema *et al.*, who varied the angularity of polyhedral particles [11,28]. But the fit can be improved by including in Eq. (35a) the cross products of the anisotropies as follows [28,59]:

$$\begin{aligned}\frac{q}{p} \simeq{}& \frac{2}{5}(a_c + a_{ln} + a_{lt} + a_{fn} + a_{ft}) \\ &+ \frac{4}{105}(a_c.a_{fn} + a_c.a_{ln} + a_{ln}.a_{fn}) \\ &+ \frac{16}{105}(a_c.a_{ft} + a_c.a_{lt} + a_{ln}.a_{ft} + a_{lt}.a_{fn}).\end{aligned} \tag{36}$$

As we see in Fig. 23, Eq. (36) gives a better approximation of q/p than Eq. (36a) but is more complicated. This indicates that the analysis of the texture and force chains in terms of the neighbor network is more relevant than that in terms of the contact network, due precisely to the role of multiple contacts. Thus, for $\eta < 0.4$ the increase in shear strength with η can be attributed to the increase in the anisotropies, and in particular, the increase in $a_{fn'}$ and $a_{ft'}$ underlies the increase in shear strength at the largest values of η despite the plateau observed for a'_c.

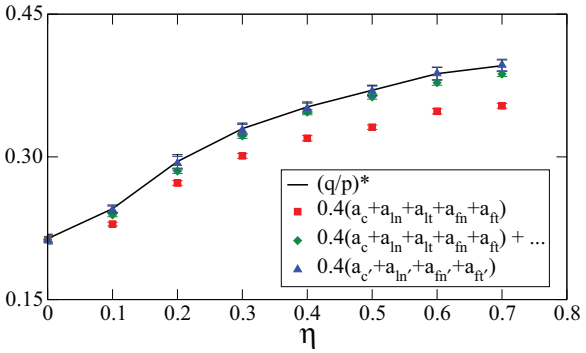

FIG. 23. (Color online) Normalized shear stress as a function of η together with harmonic approximations given by Eqs. (35) and (36). Error bars represent the standard deviation of the data.

VI. CONCLUSIONS

In this paper, a systematic analysis of the effect of shape nonconvexity on the rheological parameters of sheared granular materials has been presented by means of 3D contact dynamic simulations. Nonconvex particle shapes are modeled as aggregates of four overlapped spheres and characterized by a single parameter η, which we varied, in steps of 0.1, from 0 (spheres) to ∼0.7. Note that an aggregate of four tangent spheres corresponds to $\eta \sim 0.73$. The macroscopic and microstructural properties of several packings of 12 000 aggregates under triaxial compression in a rectangular simulation cell were analyzed as a function of η.

It was shown that the shear strength in the residual state is an increasing function of η, whereas the packing fraction increases up to a maximum value before decreasing down to values comparable to that of sphere packings. It is remarkable that these two macroscopic features are shared with other nonspherical shapes described by their degree η of deviation from circular shape. This suggests that η is a "good" low-order shape parameter for describing the shape effect. This finding also extends the results of a previous investigation with regular aggregates of three overlapped disks in two dimensions [36].

Another interesting feature of the aggregate packings is that their connectivity does not follow the packing fraction. Increasing the nonconvexity leads to an increase in multiple contacts between aggregates with essentially the same number of neighbors per particle. This microstructural property underlies the fact that the packings are increasingly looser, but with a higher shear strength. As already shown for elongated and angular particles, the case of nonconvex particles again illustrates clearly that the packing fraction and its evolution are not sufficient for description of the plastic behavior of granular media composed of nonspherical particles. The relevant internal variables as suggested by the harmonic decomposition of the stress tensor are the fabric anisotropy, normal- and radial-force anisotropies, and friction mobilization. A detailed analysis of the fabric and force anisotropies developed in the contact network and neighbor network frames allowed us to highlight the microscopic mechanisms leading to their observed dependence with respect to η.

The increase in shear strength stems from that in all anisotropies. Nevertheless, at higher levels of nonconvexity our data indicate that the force and friction anisotropies prevail compared to the fabric anisotropy, which tends to saturate. This saturation is related to both the increase in interlocked contacts (double and triple contacts) and the fact that the mean number of neighbors per particle remains constant. As a consequence, the aggregates can move only in the form of clusters, with relative sliding and rolling localized mainly at the simple contacts leading to the increase in force and friction force anisotropies. At the same time, larger pores occur due to this "clustered" motion of the aggregates, partially explaining the decrease in packing fraction observed at higher levels of nonconvexity.

Therefore, friction mobilization and interlocking appear to play a major role at high nonconvexity and more analysis should be performed specifically for highly nonconvex particles but also for other particle shapes and higher sliding friction or rolling friction between particles in order to characterize the local kinematics and clustering effects.

[1] R. Jensen, T. B. Edil, P. J. Bosscher, M. E. Plesha, and N. B. Khala, Int. J. Geomech. **1**, 1 (2001).

[2] F. Alonso-Marroquin and H. J. Herrmann, Phys. Rev. E **66**, 021301 (2002).

[3] S. Antony and M. Kuhn, Int. J. Solids Struct. **41**, 5863 (2004).

[4] W. Man, A. Donev, F. Stillinger, M. Sullivan, W. Russel, D. Heeger, S. Inati, S. Torquato, and P. Chaikin, Phys. Rev. Lett. **94**, 198001 (2005).

[5] E. Azéma, F. Radjaï, R. Peyroux, F. Dubois, and G. Saussine, Phys. Rev. E **74**, 031302 (2006).

[6] I. Zuriguel, T. Mullin, and J. M. Rotter, Phys. Rev. Lett. **98**, 028001 (2007).

[7] A. Wouterse, S. Williams, and A. Philipse, J. Phys.: Condens. Matter **19**, 406215 (2007).

[8] I. Zuriguel and T. Mullin, Proc. R. Soc. A **464**, 99 (2008).

[9] A. Jaoshvili, A. Esakia, M. Porrati, and P. M. Chaikin, Phys. Rev. Lett. **104**, 185501 (2010).

[10] E. Azéma, F. Radjaï, R. Peyroux, V. Richefeu, and G. Saussine, Eur. Phys. J. E **26**, 327 (2008).

[11] E. Azéma, F. Radjaï, and G. Saussine, Mech. Mater. **41**, 729 (2009).

[12] S. A. Galindo-Torres, F. Alonso-Marroquin, Y. C. Wang, D. Pedroso, and J. D. Muñoz Castaño, Phys. Rev. E **79**, 060301(R) (2009).

[13] R. C. Hidalgo, I. Zuriguel, D. Maza, and I. Pagonabarraga, Phys. Rev. Lett. **103**, 118001 (2009).

[14] M. Acevedo, R. C. Hidalgo, I. Zuriguel, D. Maza, and I. Pagonabarraga, Phys. Rev. E **87**, 012202 (2013).

[15] W. Lim and G. MacDowel, Gran. Matter **7**, 19 (2005).

[16] G. Saussine, C. Cholet, P. Gautier, F. Dubois, C. Bohatier, and J. Moreau, Comput. Methods Appl. Mech. Eng. **195**, 2841 (2006).

[17] J. Fourcade, P. Sornay, F. Sudreau, and P. Papet, Powder Metall. **49**, 125 (2006).

[18] M. Lu and G. McDowel, Gran. Matter **9**, 69 (2007).

[19] K. Maeda, H. Sakai, A. Kondo, T. Yamaguchi, M. Fukuma, and E. Nukudani, Gran. Matter **12**, 499 (2010).

[20] C. Nouguier-Lehon, B. Cambou, and E. Vincens, Int. J. Numer. Anal. Meth. Geomech **27**, 1207 (2003).

[21] C. Nouguier-Lebon, E. Vincens, and B. Cambou, Int. J. Solids Struct. **42**, 6356 (2005).

[22] E. Azéma, F. Radjaï, R. Peyroux, and G. Saussine, Phys. Rev. E **76**, 011301 (2007).

[23] S. A. Galindo-Torres, J. D. Muñoz, and F. Alonso-Marroquin, Phys. Rev. E **82**, 056713 (2010).

[24] E. Azéma, Y. Descantes, N. Roquet, J.-N. Roux, and F. Chevoir, Phys. Rev. E **86**, 031303 (2012).

[25] E. Azéma and F. Radjaï, Phys. Rev. E **81**, 051304 (2010).

[26] C. Nouguier-Lehon, C. R. Mecan. **338**, 587 (2010).

[27] E. Azéma, N. Estrada, and F. Radjaï, Phys. Rev. E **86**, 041301 (2012).

[28] E. Azéma, F. Radjaï, and F. Dubois, Phys. Rev. E, in press (2013).
[29] A. Donev, I. Cisse, D. Sachs, E. Variano, F. Stillinger, R. Connelly, S. Torquato, and P. Chaikin, Science **303**, 990 (2004).
[30] A. Donev, F. H. Stillinger, P. M. Chaikin, and S. Torquato, Phys. Rev. Lett. **92**, 255506 (2004).
[31] A. Donev, R. Connelly, F. H. Stillinger, and S. Torquato, Phys. Rev. E **75**, 051304 (2007).
[32] E. Nezami, Y. Hashash, D. Zaho, and J. Ghaboussi, Comput. Geotechn. **31**, 575 (2004).
[33] E. Nezami, Y. Hashash, D. Zaho, and J. Ghaboussi, Int. J. Numer. Anal. Meth. Geomech. **30**, 783 (2006).
[34] F. Radjaï and F. Dubois (eds.), *Discrete Numerical Modeling of Granular Materials* (Wiley-ISTE, New York, 2011).
[35] E. Azéma and F. Radjaï, Phys. Rev. E **85**, 031303 (2012).
[36] B. Saint-Cyr, J.-Y. Delenne, C. Voivret, F. Radjaï, and P. Sornay, Phys. Rev. E **84**, 041302 (2011).
[37] K. Szarf, G. Combe, and P. Villard, Powder Technol. **208**, 279 (2011).
[38] CEGEO, B. Saint-Cyr, K. Szarf, C. Voivret, E. Azéma, V. Richefeu, J.-Y. Delenne, G. G. Combe, C. Nouguier-Lehon, P. Villard, P. Sornay, M. Chaze, and F. Radjaï, Europhys. Lett. **98**, 44008 (2012).
[39] F. Ludewig and N. Vandewalle, Phys. Rev. E **85**, 051307 (2012).
[40] N. Estrada, E. Azéma, F. Radjaï, and A. Taboada, Phys. Rev. E **84**, 011306 (2011).
[41] J. J. Moreau, Eur. J. Mech. A/Solids **13**, 93 (1994).
[42] M. Jean, Comput. Methods Appl. Mech. Eng. **177**, 235 (1999).
[43] F. Radjaï and V. Richefeu, Mech. Mater. **41**, 715 (2009).
[44] F. Radjaï and E. Azéma, Eur. J. Env. Civil Eng. **13**, 203 (2009).
[45] V. Visseq, A. Martin, D. Iceta, E. Azéma, D. Dureisseix, and P. Alart, Comput. Mech. **49**, 709 (2012).
[46] C. Voivret, F. Radjaï, J.-Y. Delenne, and M. S. El Youssoufi, Phys. Rev. Lett. **102**, 178001 (2009).
[47] F. Radjaï, M. Jean, J. J. Moreau, and S. Roux, Phys. Rev. Lett. **77**, 274 (1996).
[48] L. Staron and F. Radjai, Phys. Rev. E **72**, 041308 (2005).
[49] L. Staron, F. Radjaï, and J. Vilotte, Eur. Phys. J. E **18**, 311 (2005).
[50] A. Taboada, K. J. Chang, F. Radjai, and F. Bouchette, J. Geophys. Res. **110**, 1 (2005).
[51] N. Estrada, A. Taboada, and F. Radjaï, Phys. Rev. E **78**, 021301 (2008).
[52] M. Boton, E. Azéma, N. Estrada, F. Radjaï, and A. Lizcano, Phys. Rev. E **87**, 032206 (2013).
[53] Note that video samples of the simulations analyzed in this paper can be found by following this link: www.cgp-gateway.org/Video/ref022.
[54] C. Voivret, F. Radjaï, J.-Y. Delenne, and M. S. El Youssoufi, Phys. Rev. E **76**, 021301 (2007).
[55] GDR-MiDi, Eur. Phys. J. E **14**, 341 (2004).
[56] J.-N. Roux, Phys. Rev. E **61**, 6802 (2000).
[57] H. Troadec, F. Radjaï, S. Roux, and J.-C. Charmet, Phys. Rev. E **66**, 041305 (2002).
[58] A. Mirghasemi, L. Rothenburg, and E. Maryas, Geotechnique **52**, 209 (2002).
[59] H. Ouadfel and L. Rothenburg, Mech. Mater. **33**, 201 (2001).
[60] D. M. Mueth, H. M. Jaeger, and S. R. Nagel, Phys. Rev. E. **57**, 3164 (1998).
[61] P. T. Metzger, Phys. Rev. E **70**, 051303 (2004).
[62] L. E. Silbert, Phys. Rev. E **74**, 051303 (2006).